JOM, Vol. 75, No. 12, 2023
https://doi.org/10.1007/s11837-023-06175-w

Facile Synthesis of CoO/Sm_2O_3@UiO-66-NH_2/NF Composite as Efficient Photocatalysts for Oxygen Evolution Reaction

MUHAMMAD KASHIF,[1] MUHAMMAD FIAZ,[2] SUMAIRA MANZOOR,[1] MUHAMMAD NAJAM-UL-HAQ,[1] MUHAMMAD ASIM FARID,[3] and MUHAMMAD ATHAR[1,4]

1.—Institute of Chemical Sciences, Bahauddin Zakaryia University, Multan 60800, Pakistan. 2.—Department of Chemistry, Ajou University, Suwon 16499, Republic of Korea. 3.—Department of Chemistry, Division of Science and Technology, University of Education, Lahore, Pakistan. 4.—e-mail: athar.qr@bzu.edu.pk

Developing efficient metal-organic framework (MOF)-based photoelectro-catalysts towards oxygen evolution reaction (OER) has gained much research attention due to their unique properties, like high surface area, tunable pore size, and flexible pore size structure. In the present study, we report the facile synthesis of highly efficient MOF-based photoelectro-catalysts via incorporation of as-synthesized Sm_2O_3-based nanomaterials into Zr-based MOF-UiO-66-NH_2 through the solvothermal method. All the synthesized materials are characterized via different analytical techniques. Among them, CoO/Sm_2O_3@UiO-66-NH_2/NF exhibited efficient oxygen evolution (OER) activity, and it delivers 10 mA cm^{-2} current density at just 254 mV overpotential, with a lower Tafel slope value of 92 mV dec^{-1}. Further, it was revealed that incorporating nanomaterials has improved the catalytic OER activity due to synergistic effect and hetero-junction formation. Furthermore, CoO/Sm_2O_3@UiO-66-NH_2 has exhibited excellent stability, as there is negligible degradation in the current density before and after 1000th linear voltammetry sweeps. Based on these observations, it is believed that this study will trigger the development of more low overpotential MOFs-based OER photoelectro-catalysts.

INTRODUCTION

Recently, energy demand has been a significant challenge for society and the scientific era. Scientists' exploration for safe, clean, and renewable energy resources can overcome the expected deficiency of non-renewable energy resources.[1] Hydrogen is a favorable, clean, renewable, and safe fuel that, upon burning, does not emit pollutants. It is used in many electric devices, vehicles, aircraft, and spacecraft impulsion, and can be captured into hydrocarbons, water, and other organic matters. Hydrogen is separated from these compounds and especially from water, by using different techniques, among which the water-splitting method is excellent at extracting hydrogen from water. Various methods have been introduced for the water-splitting process, such as photoelectrochemical (PEC), photocatalytic, photobiological, radiolysis, and thermal decomposition.[2–5] In this regard, the PEC has made remarkable progress in producing hydrogen from water.[6,7] However, water splitting is a two-step reaction; hydrogen evolution reaction (HER) and oxygen evolution reaction (OER); both of these processes, especially OER, require much overpotential.[8] So, the development of a low overpotential OER catalyst is urgently required. Different effective photocatalytic materials have been reported for water splitting towards OER and HER. Among these, a class of porous materials known as metal-organic frameworks (MOFs) has emerged as efficient catalytic materials for OER.[9] Due to their unique properties such as high porosity, structural diversity, tunable pore size, and the large surface

(Received May 28, 2023; accepted September 25, 2023; published online October 31, 2023)

area, they are using used in vast applications, such as gas separation/adsorption, chemical sensing, luminescence, magnetism, proton conductivity, biomedicine, energy storage, and energy conversion.[10–16] Zirconium-based MOFs UiO-66 exhibit high thermal and chemical stability up to 500°C.[17] Under ultraviolet light irradiation, UiO-66 was used for water splitting in 2010 by Garcia and co-workers.[18] However, UiO-66 does not respond effectively to visible light and its efficiency is increased by incorporating Pt nanoparticles. It has been observed that Pt@UiO-66 has exhibited better and improved catalytic activity towards water splitting compared to bare UiO-66.[19] Yuan and co-workers introduced a system in 2015 using erythrosine B dye to sensitize UiO-66 for high hydrogen production.[20] Further, the catalytic activity of UiO-66 is increased by amine functionalization, and it is observed that UiO-66-NH_2 has shown better OER and HER activity compared to bare UiO-66.[21] The activity of UiO-66-NH_2 is further improved via the incorporation of Pt nanoparticles, and Pt@UiO-66-NH_2 has emerged as an efficient catalyst towards water splitting.[22] Nowadays, rare earth metal oxide nanoparticles are effectively used in photocatalytic applications due to their suitable band alignment. Among these, samarium, europium, cerium, and yttrium nanomaterials are showing significant performance in various applications such as selective electrodes and high-efficiency phosphors.[23,24]

Therefore, considering the above discussion, a simple and facile synthesis route has been used for designing highly efficient Sm_2O_3-based nanomaterials@UiO-66-NH_2 catalysts for OER. Among all the synthesized materials, CoO/Sm_2O_3@UiO-66-NH_2 has emerged as efficient catalytic material towards OER. It delivers 10-mA cm^{-2} current density at just 254 mV overpotential with a lower Tafel slope (92 mV dec^{-1}). The activity is superior to many previously reported precious and non-precious metal-based OER catalysts.[25–41]

EXPERIMENTAL

Chemicals

The chemicals used are samarium sulfate octahydrate ($Sm_2(SO_4)_3{\cdot}8H_2O$, > 99.9%; Merck), ammonium hydroxide (NH_4OH, 30.0%; Merck), titanium(IV) oxysulfate ($TiOSO_4$, 99.9%; Sigma Aldrich), cobalt (II) chloride hexahydrate ($CoCl_2{\cdot}6H_2O$, 99%; Merck), N,N-dimethylformamide (DMF, 99%), zirconium (IV) tetrachloride ($ZrCl_4$, 99.9%, Sigma Aldrich), 2-aminoterephthalic acid (99%, Sigma Aldrich) and polyethylene glycol (PEG). All the chemicals were used as obtained without any further purification for the synthesis of materials.

Synthesis of Sm_2O_3 Nanoparticles

Sm_2O_3 nanoparticles were synthesized by using the hydrothermally-assisted calcination method.[42] In a typical reaction, a 0.02-M (30-mL) solution of $Sm_2(SO_4)_3{\cdot}8H_2O$ was prepared in distilled water under stirring for 15 min. Then, 5 mL of ammonium hydroxide was added dropwise into the above mixture, and then PEG was added as a surfactant to form the precipitates. The resultant mixture was transferred to a stainless steel autoclave and placed in an oven at 150°C for 12 h. After completing the reaction, the product was obtained by centrifugation and washed with distilled water multiple times. The dried precipitates were calcinated at 400°C for 5 h to obtain the Sm_2O_3 nanoparticles.

Synthesis of TiO_2/Sm_2O_3 and CoO/Sm_2O_3 Nanocomposite

The TiO_2/Sm_2O_3 and CoO/Sm_2O_3 composites were synthesized by using the same hydrothermally-assisted calcination method as mentioned above with the addition of 0.19 g of $TiOSO_4$ (for TiO_2/Sm_2O_3) and 0.28 g of $CoCl_2{\cdot}6H_2O$ (for CoO/Sm_2O_3) in a 0.02-M solution (0.81 g/30 mL) of $Sm_2(SO_4)_3{\cdot}8H_2O$ prior to the addition of ammonium hydroxide.

Incorporation of Synthesized Materials into UiO-66-NH_2

The synthesized materials were incorporated into UiO-66-NH_2 by following the one-step solvothermal method. For this, 10 mL DMF suspension of nanomaterials (0.20 g) was added into 20 mL DMF solution of zirconium (IV) tetrachloride (1.39 g), followed by dropwise addition of 20 mL solution of 2-aminoterephthalic acid (1.08 g) under stirring. Then, the whole mixture was transferred into an autoclave and kept at 120°C for 24 h. After that, the product was separated by centrifugation, washed with DMF and dried. For comparison purposes, the bare UiO-66-NH_2 was also synthesized using the same procedure without adding the nanomaterials.

Characterization

The shape and morphology of all the synthesized samples were studied by using scanning electron microscopy (SEM; JSM-6480LV; JEOL) with attached energy dispersive X-ray spectroscopy (EDX). Powder X-ray diffraction (PXRD; D-8 Advance; Bruker) patterns were recorded with Cu Kα radiation (λ = 0.15406 nm) for structural information and phase purity. Fourier-transform infrared (FTIR; IR Prestige-21; Shimadzu) spectra were obtained for functional group analysis. The UV-Vis spectra were measured by using a UV-2600 spectrophotometer for the determination of the band alignment.

Fabrication of Working Electrodes

The synthesized samples (0.01 g) in 100 μL were sonicated for 15 min and then deposited on already dried and cleaned 1 cm^2 nickel foam (NF) pieces via

the drop cast method. The loaded NF was then used as working electrodes.

Photoelectrochemical Studies for Oxygen Evolution Reaction (OER)

Photoelectrochemical studies towards OER were performed in a standard three-electrode setup controlled by a Uniscan workstation. A typical three-electrode setup consists of Pt-wire as the counter electrode, Ag/AgCl as the reference electrode, and synthesized materials@NF as the working electrode. OER analysis was carried out by performing cyclic voltammetric and linear sweep voltammetric measurements at scan rates of 10 mVs^{-2} and 5 mVs^{-2}, respectively, in 1 M KOH electrolyte in the dark as well as in the presence of visible light. The obtained potential was then converted into a reversible hydrogen electrode (RHE). Further, impedance was measured at an applied potential of 0.3 V to measure the resistance in electron transfer towards OER.

RESULTS AND DISCUSSION

Morphological Analysis

The morphology of the as-synthesized samples was studied by SEM, as shown in Fig. 1a, b, c, and d. The SEM image of UiO-66-NH_2 shows uniformly dispersed block-shape morphology with 1339-nm average particle size and smooth surfaces. A similar morphology with rough surfaces was found for the incorporated materials with a decrease in average particle size giving 297 nm, 448 nm, and 266 nm for Sm_2O_3@UiO-66-NH_2, TiO_2/Sm_2O_3@UiO-66-NH_2, and CoO/Sm_2O_3@UiO-66-NH_2, respectively (Fig. 1b, c, and d). Thus, after incorporation, a decrease in particle size was observed, and therefore incorporated particles may have higher surface area and higher catalytic activity compared to bare MOF.

This reveals that the incorporation of nanomaterials has decreased the particle size and increased the surface area, which will enhance the catalytic-OER activity as observed during the photoelectrochemical studies discussed below. Furthermore, it is also observed that all the synthesized samples are uniformly dispersed without agglomeration. The EDX spectra of UiO-66-NH_2, Sm_2O_3@UiO-66-NH_2, TiO_2/Sm_2O_3@UiO-66-NH_2, and CoO/Sm_2O_3@UiO-66-NH_2 show Zr, C, O, and N peaks of UiO-66-NH_2 as well as the Sm peak indexed to the Sm_2O_3 nanoparticles, Ti to TiO_2/Sm_2O_3 and Co to CoO/Sm_2O_3, as shown in Fig. 2a, b, c, and d.

Structural Analysis

PXRD was used to analyze the structure and purity of all the synthesized samples. PXRD patterns of the samples with a simulated pattern of the host UiO-66-NH_2 are shown in Fig. 3a, and show that all the materials are grown in a well-crystallized form. It can be seen that the major peaks in the PXRD pattern of the synthesized UiO-66-NH_2 MOF during this study are matched well with the simulated pattern of this MOF. Similarly, the PXRD patterns of all the functionalized materials are matched well with the simulated pattern of the as-synthesized UiO-66-NH_2. Some variations are observed in the PXRD pattern of CoO/Sm_2O_3@UiO-66-NH_2, which might be due to slight changes in the crystal lattice of UiO-66-NH_2 due to interaction between the incorporated CoO/Sm_2O_3 nanocomposite and UiO-66-NH_2. However, such variations are not observed in the PXRD patterns of Sm_2O_3@UiO-66-NH_2 and TiO_2/Sm_2O_3@UiO-66-NH_2, which reveals that incorporating Sm_2O_3 and TiO_2/Sm_2O_3 does not affect the crystalline structure of the host UiO-66-NH_2. However, the PXRD patterns of the CoO/Sm_2O_3@UiO-66-NH_2, Sm_2O_3@UiO-66-NH_2, and TiO_2/Sm_2O_3@UiO-66-NH_2 reveal that all the diffraction peaks are indexed to UiO-66-NH_2 and its peaks, and that there are no visible peaks for the CoO/Sm_2O_3, Sm_2O_3 and TiO_2/Sm_2O_3 nanoparticles. This is because their peaks are masked by the UiO-66-NH_2.

Figure 3b shows the FTIR spectra of the synthesized samples within the wavenumber range 4000–500 cm^{-1}. The FTIR spectrum of the as-synthesized UiO-66-NH_2 matches well with the reported patterns, and all the characteristic vibrational peaks are indexed to UiO-66-NH_2.[43,44] In the FTIR spectrum of UiO-66-NH_2, four characteristic vibrational peaks are observed at 1248 cm^{-1}, 1374 cm^{-1}, 1563 cm^{-1}, and 1646 cm^{-1} due to the stretching vibrational motions of primary amine (-NH_2), the symmetric as well as asymmetric vibrational motions of carboxylic acid, and a free aromatic carboxylic acid, respectively.[45] Another small vibrational peak is also observed at 770 cm^{-1} due to Zr-O vibrational motion.[46] In the same way, the FTIR spectra of incorporated materials also contain the same vibrational peaks, as in bare MOF, with an additional peak at 1092 cm^{-1} due to Sm-O-Sm stretching vibrational motion, as already reported.[47] Thus, this reveals the successful incorporation of Sm_2O_3-based nanomaterials in the host MOF.

Figure 4a shows the UV-Vis spectra of all the synthesized materials, measured within the wavelength range 200–900 nm.

The UV-Vis spectrum of bare MOF (UiO-66-NH_2) shows absorption in both the UV and visible-region with λ_{max} at 220 nm and 300 nm, respectively. Its absorption edge ends at about 486 nm. However, in the UV–Vis spectra of the incorporated materials, an extension of absorption towards the visible region is observed. The maximum extension is observed in CoO/Sm_2O_3@UiO-66-NH_2 with λ_{max} at 267 nm and 358 nm for the UV and the visible regions, respectively, and the absorption edge extends up to 585 nm. This means that functionalization has enhanced the absorption in the visible

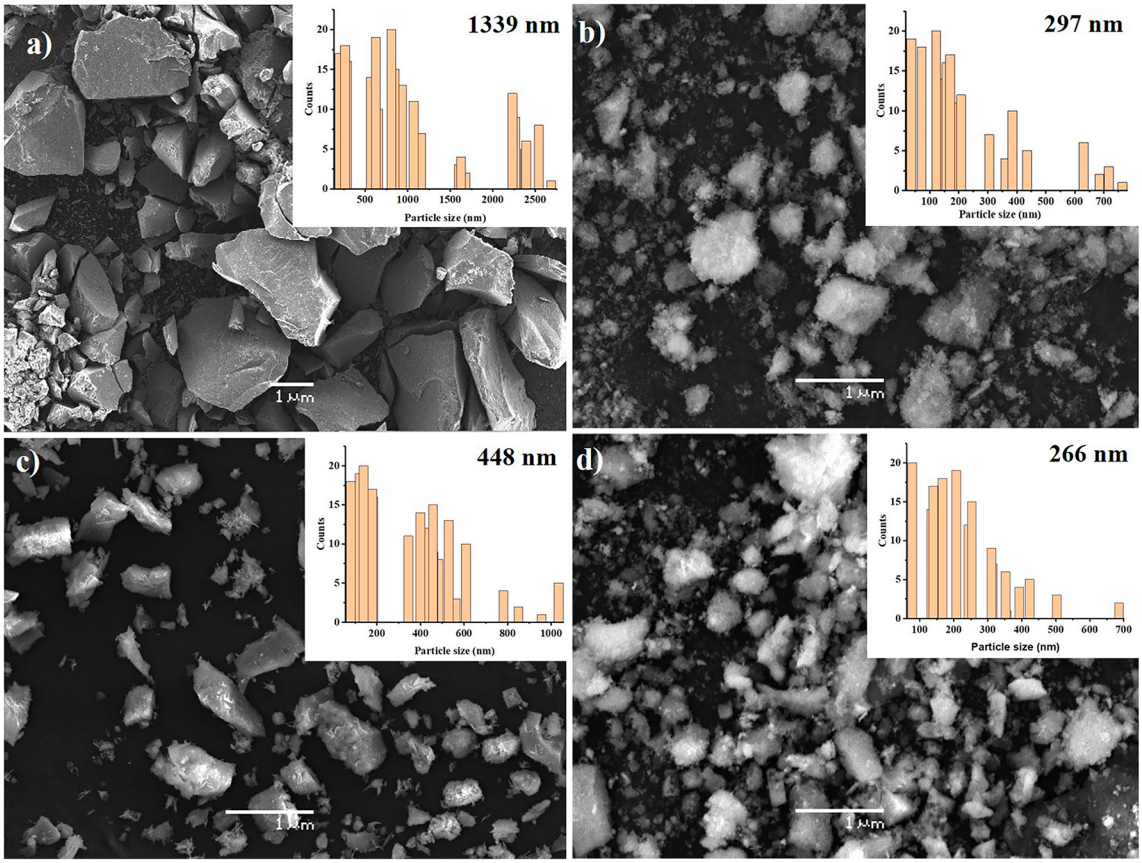

Fig 1. SEM images of (a) UiO-66-NH_2, (b) Sm_2O_3@UiO-66-NH_2, (c) TiO_2/Sm_2O_3@UiO-66-NH_2, and (d) CoO/Sm_2O_3@UiO-66-NH_2.

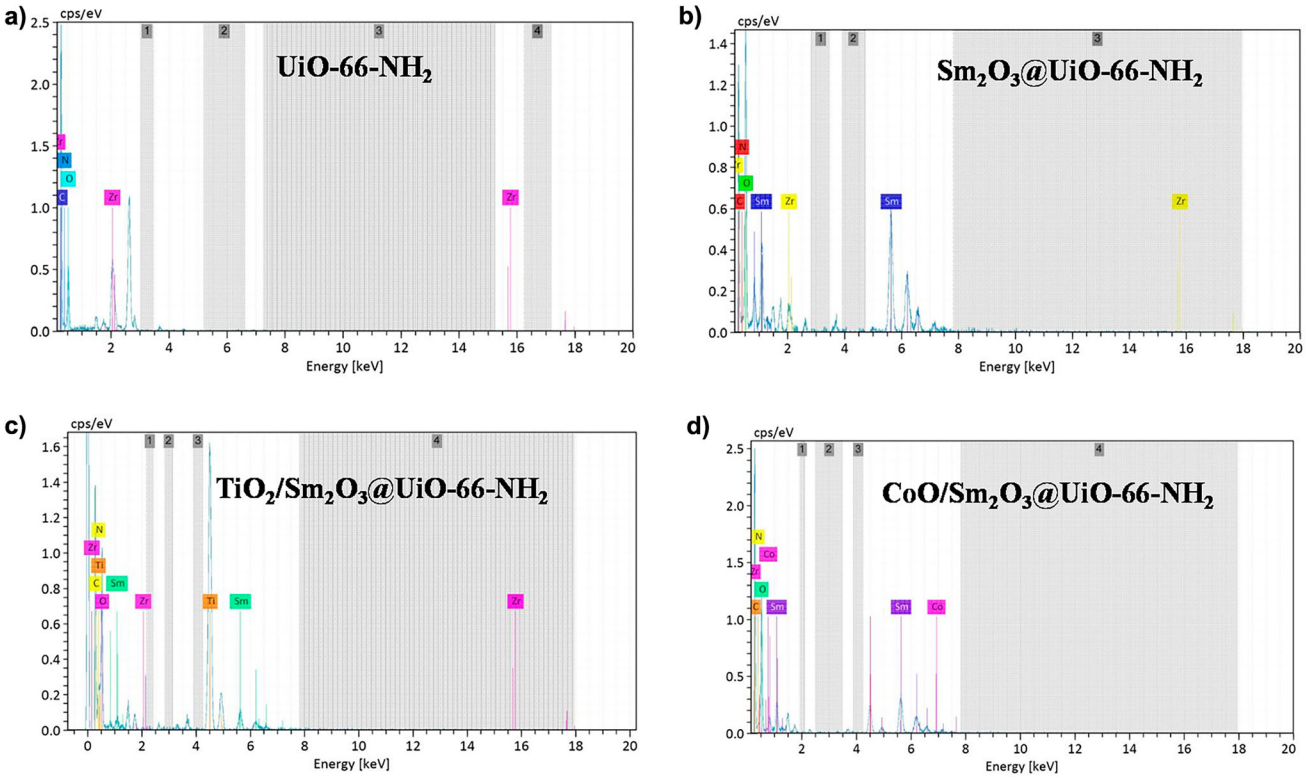

Fig 2. EDX spectra of (a) UiO-66-NH_2, (b) Sm_2O_3@UiO-66-NH_2, (c) TiO_2/Sm_2O_3@UiO-66-NH_2, and (d) CoO/Sm_2O_3@UiO-66-NH_2.

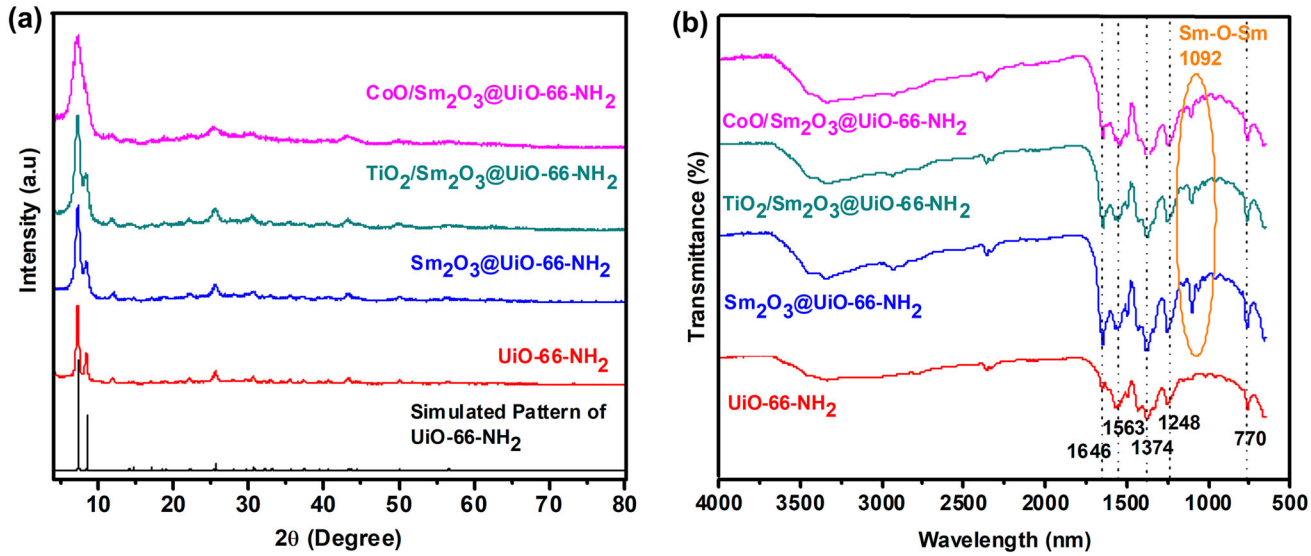

Fig 3. (a) PXRD patterns and (b) FTIR spectra of as-synthesized UiO-66-NH_2, Sm_2O_3@UiO-66-NH_2, TiO_2/Sm_2O_3@UiO-66-NH_2, and CoO/Sm_2O_3@UiO-66-NH_2.

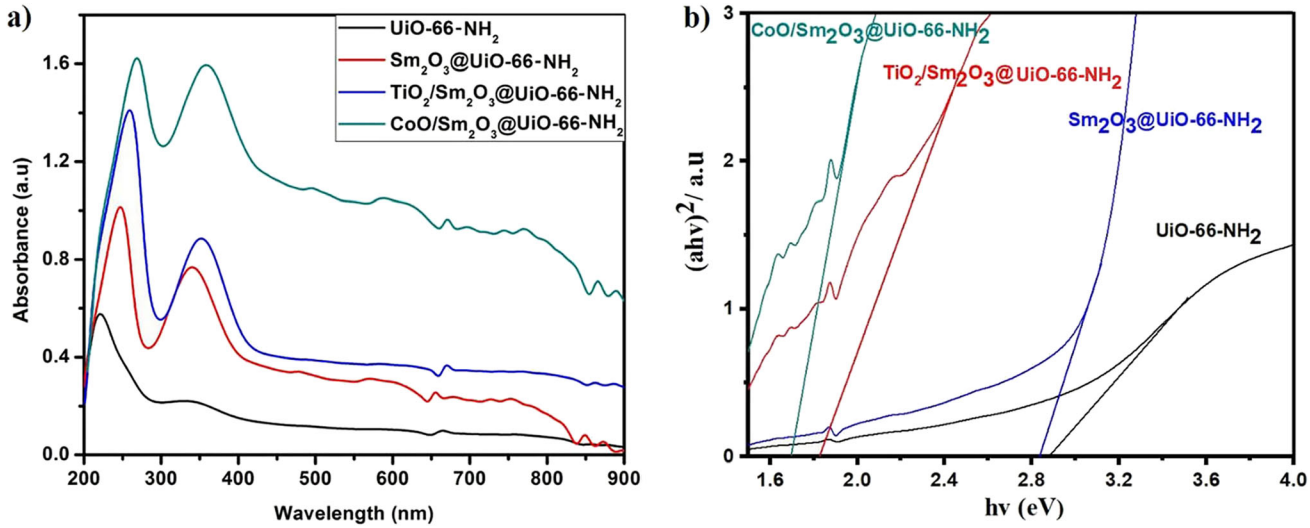

Fig 4. (a) UV-Vis spectra and (b) Tauc plot of UiO-66-NH_2, Sm_2O_3@UiO-66-NH_2, TiO_2/Sm_2O_3@UiO-66-NH_2, and CoO/Sm_2O_3@UiO-66-NH_2.

region which can improve the catalytic activity towards OER under visible light illumination.

The band gap energy of as-synthesized materials is obtained by linear extra-plotting of the Tauc plot, which is shown in Fig. 4b. The Tauc plot is derived from the UV-Vis spectra by using:

$$\alpha h\nu \propto A(h\nu - E_g)^{0.5} \quad (1)$$

where (α), ($h\nu$), (A), and (E_g) are constant values, α is the absorbance, $h\nu$ the energy, A the absorption coefficient, and E_g is used for the band gap. The obtained band gap energies of UiO-66-NH_2, Sm_2O_3@UiO-66-NH_2, TiO_2/Sm_2O_3@UiO-66-NH_2, and CoO/Sm_2O_3@UiO-66-NH_2 are 2.88 eV, 2.83 eV, 1.82 eV, and 1.68 eV, respectively. Thus, these demonstrate that incorporating the nanomaterials has shifted the band gap energy towards a more visible region, and has decreased the rate of photo-generated electron–hole pair recombination by hetero-junction formation between the incorporated nanomaterials and UiO-66-NH_2. Hence, incorporation has improved the catalytic activity towards OER.

Photoelectrochemical Studies Towards Oxygen Evolution Reaction (OER)

All the catalytic activities towards OER have been measured in 1.0 M KOH alkaline solution and compared with previously reported OER catalysts.[25–41] The OER-catalytic activity was performed by CV and LSV measurements at scan rated of 10 mVs^{-1} and 5 mVs^{-1}, respectively, in the dark and in visible light. Figure 5a shows the CV

curves of the as-synthesized samples. As expected, no noticeable current is obtained in the dark, and efficient activity is observed in the presence of visible light. The bare UiO-66-NH_2/NF exhibits poor activity and produces negligible current density (0.073 mA cm^{-2}), as shown in Supplementary Figure S1. To increase its activity, CoO-Sm_2O_3 was incorporated into the MOF, and an interface was developed between the MOF and the incorporated materials via a heterojunction, which facilitates efficient electron transfer, increases the charge separation, and increases OER activity. Thus, the incorporated materials exhibit efficient activity towards OER. Among the synthesized samples, CoO/Sm_2O_3@UiO-66-NH_2/NF exhibits maximum OER activity and generates a maximum current density of 275.51 mA cm^{-2} compared to TiO_2/Sm_2O_3@UiO-66-NH_2/NF (222.04 mA cm^{-2}) and Sm_2O_3@UiO-66-NH_2 (211.91 mA cm^{-2}).

Figure 5b shows the LSV curves of all the synthesized samples within the RHE potential range 1.0–2.0 V. Like the CV, no activity was observed in the dark and efficient activity was observed in the presence of visible light. The functionalized materials show better activity compared to the bare MOF. The CoO/Sm_2O_3@UiO-66-NH_2 exhibited the lowest onset potential of 1.47 V versus RHE compared to other samples, and yielded a benchmark 10 mA cm^{-2} current density at just 254 mV overpotential compared to Sm_2O_3@UiO-66-NH_2/NF (η_{10} = 327 mV) and TiO_2/Sm_2O_3@UiO-66-NH_2/NF (η_{10} = 270 mV). It is also superior to previously reported precious and non-precious metal-based OER catalysts, such as RuO_2@Au (η_{10} = 320 mV), IrO_x (η_{10} = 320 mV), and FeP-rGO (η_{10} = 280 mV).[48,49]

Figure 5c shows the Tafel plot, η versus log j, for CoO/Sm_2O_3@UiO-66-NH_2 to understand the kinetics of OER. The CoO/Sm_2O_3@UiO-66-NH_2/NF exhibits a lower Tafel slope value, 92 mV dec^{-1}, which is comparable with previously reported OER catalysts, such as FeP-rGO(50:50)@CFP (174.9 mV dec^{-1}) and

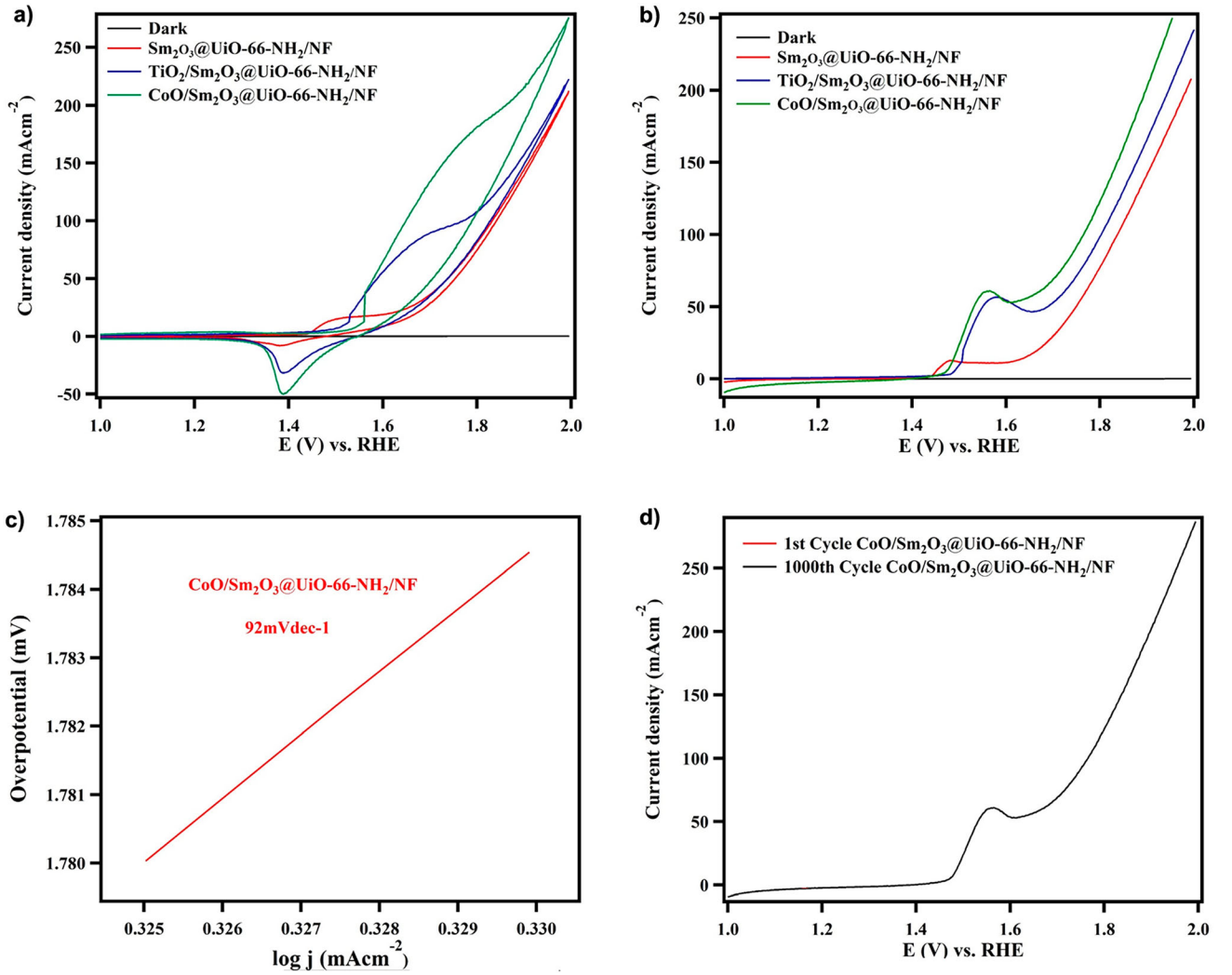

Fig 5. (a) CV, (b) LSV curves of Sm_2O_3@UiO-66-NH_2/NF, TiO_2/Sm_2O_3@UiO-66-NH_2/NF, and CoO/Sm_2O_3@UiO-66-NH_2/NF at 10 mV/s^{-1}, (c) Tafel plot of CoO/Sm_2O_3@UiO-66-NH_2/NF, and (d) stability of CoO/Sm_2O_3@UiO-66-NH_2/NF after 1000 LSV cycles.

FeP-rGO(50:50)@Au (85.2 mV dec^{-1}).[49] This lower Tafel slope value indicates the more effortless electron transfer and better OER activity. Based on the above observations, it can be concluded that incorporation has increased the catalytic OER activity of the host MOF, and CoO/Sm_2O_3/UiO-66-NH_2/NF has emerged as an efficient OER-catalyst as it showed the lowest OER onset potential, required the lowest overpotential@10 mA cm^{-2}, generated maximum current density, and exhibited a lower Tafel slope value. The stability of CoO/Sm_2O_3/UiO-66-NH_2 was investigated through the 1000th continuous LSV sweeps at 50 m Vs^{-1}. Figure 5d shows the 1st and 1000th LSV curves with negligible current degradation, indicating satisfactory CoO/Sm_2O_3@UiO-66-NH_2/NF stability.

CoO/Sm_2O_3@UiO-66-NH_2 has the lowest onset potential and maximum photocurrent density among all the samples. The obvious rationalization for this can be found in the largest width of the space charge region. The Nyquist plots of all the synthesized materials are shown in Fig. 6a and b. The material with a smaller semicircle has the lowest R_{ct} value compared to the other samples. The Nyquist plots of TiO_2/Sm_2O_3@UiO-66-NH_2 and CoO/Sm_2O_3@UiO-66-NH_2 are shown separately in Fig. 6b. The CoO/Sm_2O_3@@UiO-66-NH_2 shows the lowest interfacial charge transfer resistance (R_{ct}) compared to the other samples, as can be seen in the Nyquist plots of the photo-anodes in Fig. 6b. This confirms the formation of a *p–n* junction due to the combination of *p*-type CoO/Sm_2O_3 with *n*-type UiO-66-NH_2. These effects demonstrate that the charge carrier density is lower. The Ni foam included in the CoO/Sm_2O_3@UiO-66-NH_2 matrix provides electrochemically active sites for better surface water oxidation kinetics, which is another explanation for the composite's improved activity. Obviously, both these parameters are highly connected, resulting in CoO/Sm_2O_3@UiO-66-NH_2 having more activity than the other samples investigated (Table I).

Possible Electron Transfer and Charge Separation

Figure 5a and b shows that CoO/Sm_2O_3@UiO-66/NF has maximum catalytic activity towards OER under visible light illumination compared to all other synthesized materials. The possible electron transfers and charge separation during catalytic OER can be explained by possible electron transfer and charge separation between the MOF and the nanomaterials, as shown in Fig. 7. In the MOFs, the organic ligand acts as an antenna and captures the visible light under visible light illumination, and transfers the photoexcited electrons to a central metallic cluster.[9] In the case of CoO/Sm_2O_3@UiO-66/NF, the incorporated nanoparticles develop an interface via heterojunction formation with a central metallic cluster. The interface formation facilitates the efficient charge separation between the MOF and the incorporated materials.

Thus, during photoelectrochemical OER, under visible light illumination, the photoexcited electrons are transferred from the central metallic cluster to incorporate CoO/Sm_2O_3, and then to the counter electrode (Ag/AgCl) for hydrogen evolution. Meanwhile, the photogenerated holes are left on the working electrode (CoO/Sm_2O_3@UiO-66-NH_2), which causes water oxidation to oxygen evolution.

Effect of Incorporation upon Morphology and Photocatalytic Activity

As shown in the SEM image of bare UiO-66-NH_2, it has grown in a well-defined and uniformly dispersed block-shape morphology with smooth

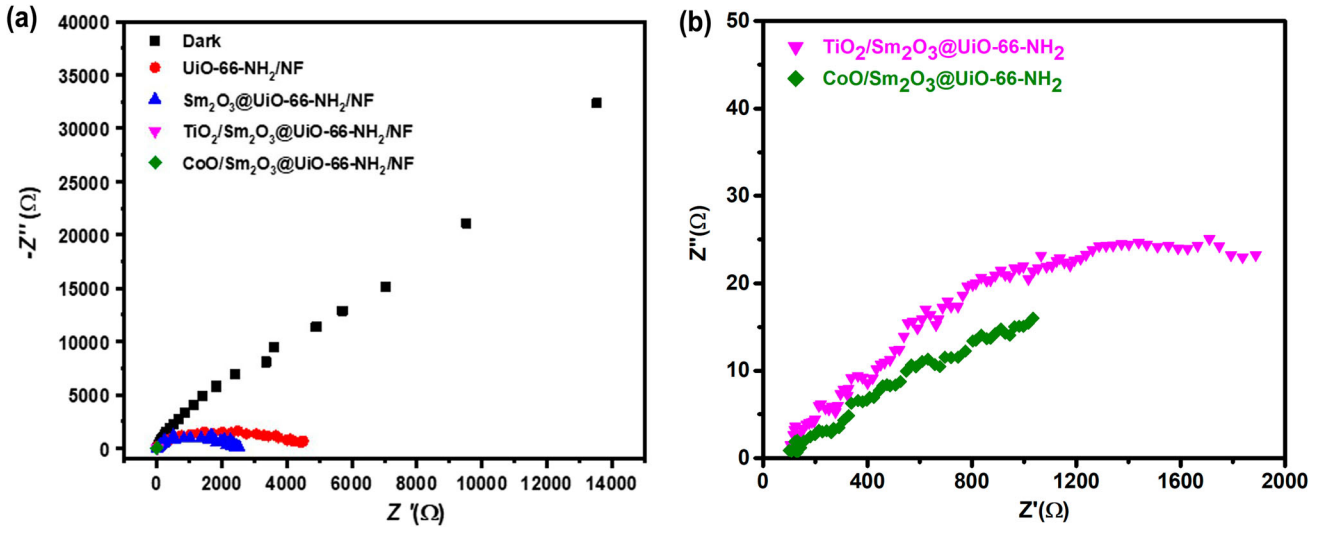

Fig 6. Nyquist plots of all the synthesized products in the dark and in the presence of light.

Table I. Comparison of CoO/Sm_2O_3@UiO-66-NH_2 with previously reported OER catalysts

Catalyst	Electrolyte	Overpotential (η_{10}) (mV)	Reference
NiCoP/C nanotubes		330	25
N-NiFeOOH	1.0 M KOH	320	26
N-NiFeOOH	1.0 M KOH	320	26
$Co_{0.5}Fe_{0.125}Mn_{0.375}WO_4$	1.0 M KOH	460	27
Co@Co_3O_4 from ZIF-67	0.1 M KOH	410	28
Co_3O_4/NPC derived from ZIF-67/COF		330	29
NiFe-NS	1.0 M KOH	304	30
CoP@RGO	1.0 M KOH	280	31
$CeO_2/CoSe_2$	0.1 M KOH	288	32
Co_3O_4/Co-Fe oxide $DSNB_S$	1.0 M KOH	297	33
CoCH/NF	1.0 M KOH	332	34
NiFe-NS	1.0 M KOH	304	30
CuO@UiO-66-NH_2/NF	1.0 M KOH	283	35
Co_3O_4/NF	1.0 M KOH	368	36
$MnCo_2O_4$/GC	1.0 M KOH	390	37
$(Ni_2CO_1)_{0.925}Fe_{0.075}$MOF/NF	1.0 M KOH	257	38
FeNi@NCNT		300	39
$CoTe_2$@NCNTFs		330	40
CoO_x/UiO-66	1.0 M KOH	283	41
NiO/UiO-66	1.0 M KOH	291.6	41
CoO/Sm_2O_3@UiO-66-NH_2/NF	1.0 M KOH	254	This work

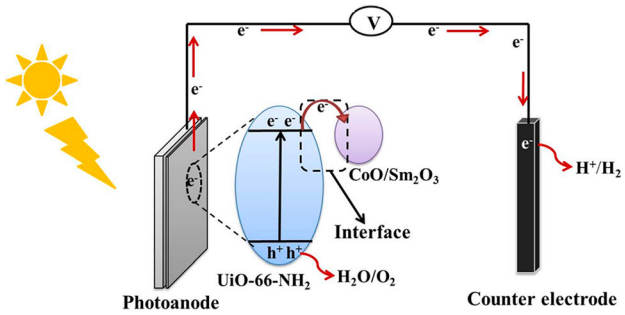

Fig 7. Possible electron transfer and charge separation during photoelectrochemical OER.

surfaces, and exhibits an almost similar morphology after in situ incorporation of the nanomaterials. The incorporation of nanomaterials into UiO-66-NH_2 results in a decrease in average particle size and makes the crystal surfaces rough. UiO-66 and its derivatives have been used for both OER and HER reactions in water splitting.[18,19,21,41,50] Garcia and co-workers found poor activity of UiO-66 for water splitting under ultraviolet light irradiation.[18] The catalytic activity of UiO-66 was increased by amine functionalization, and UiO-66-NH_2 showed better OER and HER activity compared to bare UiO-66.[21] Charles improved the activity of UiO-66 via the incorporation of CoO_x and NiO nanoparticles, and (CoO_x/UiO-66 and NiO/UiO-66) heterostructures emerged as efficient catalysts towards the oxygen evolution reaction.[41] The MoS_2/UiO-66 hybrid delivers 10 mA cm^{-2} current density at just 180 mV overpotential for the OER.[50] The Pt@UiO-66 exhibited better HER catalytic activity compared to bare UiO-66.[25] This indicates that the incorporation of nanoparticles into UiO-66-NH_2 develops the heterojunction and increases the electrocatalytic activity of UiO-66-NH_2 against the oxygen evolution reaction. Our synthesized Sm_2O_3@UiO-66-NH_2 and TiO_2/Sm_2O_3@UiO-66-NH_2 required 327 mV and 270 mV overpotential, respectively, to deliver 10 mA cm^{-2} current density. CoO/Sm_2O_3@UiO-66-NH_2 compared to other samples yielded a benchmark 10 mA cm^{-2} current density at just 254 mV overpotential. Thus, the OER activity of UiO-66-NH_2 has been enhanced due to heterojunction formation between the incorporated CoO/Sm_2O_3 and UiO-66-NH_2 which is far better than the reported materials. These findings divert more attention to synthesize new materials as catalysts for water splitting.

CONCLUSION

The facile synthesis of highly efficient MOF-based OER catalyst via incorporating Sm_2O_3-based nanomaterials into the host MOF UiO-66-NH_2 by solvothermal method is reported. All the synthesized materials have been characterized by PXRD, SEM, FTIR, and UV-Visible spectroscopy. The results indicate the successful synthesis of UiO-66-NH_2 and nanomaterials@UiO-66-NH_2. It has also been observed that incorporating the nanomaterials has shifted the band gap energy more towards the visible region, reduced electron–hole pair recombination, increased the absorption of visible light, and enhanced the OER activity. The catalytic OER activities of the synthesized materials were studied

in an alkaline solution via CV and LSV measurements. Among all the synthesized materials, CoO/Sm_2O_3@UiO-66-NH_2 has emerged as an efficient OER catalyst as it requires just 254 mV overpotential to deliver the benchmark 10 mA cm^{-2} current density, with a lower Tafel slope value of 92 mV dec^{-1} in the presence of visible light. Therefore, this study encourages the development of a more efficient MOF-based OER catalyst.

SUPPLEMENTARY INFORMATION

The online version contains supplementary material available at https://doi.org/10.1007/s11837-023-06175-w.

ACKNOWLEDGEMENTS

The authors acknowledge the Institute of Chemical Sciences, Bahauddin Zakaryia University, Pakistan for facilitating laboratory facilities to carry out this project.

CONFLICT OF INTEREST

The authors declare that they have no conflict of interest.

REFERENCES

1. B. Parida, S. Iniyan, and R. Goic, *Renew. Sustain. Energy Rev.* 15, 1625 (2011).
2. K. Maeda, and K. Domen, *J. Phys. Chem. Lett.* 1, 2655 (2010).
3. A. Cecal, A.O. Paraschivescu, K. Popa, D. Colisnic, G.A. Timco, and L. Singenerean, *J. Serb. Chem. Soc.* 68, 593 (2003).
4. I. Akkerman, M. Janssen, J. Rocha, and R.H. Wijffels, *Int. J. Hydrogen Energy* 27, 1195 (2002).
5. J. Lede, F. Lapicque, and J. Villermaux, *Int. J. Hydrogen Energy* 8, 675 (1983).
6. C. Jiang, S.J. Moniz, A. Wang, T. Zhang, and J. Tang, *Chem. Soc. Rev.* 46, 4645 (2017).
7. W.-J. Ong, L.-L. Tan, Y.H. Ng, S.-T. Yong, and S.-P. Chai, *Chem. Rev.* 116, 7159 (2016).
8. X. Xiao, L. Yang, W. Sun, Y. Chen, H. Yu, K. Li, B. Jia, L. Zhang, and T. Ma, *Small* 18, 2105830 (2022).
9. F. Song, W. Li, and Y. Sun, *Inorganics*. https://doi.org/10.3390/inorganics5030040 (2017).
10. Z. Lu, J. Zhang, H. He, L. Du, and C. Hang, *Inorg. Chem. Front.* 4, 736 (2017).
11. X.Z. Song, S.Y. Song, S.N. Zhao, Z.M. Hao, M. Zhu, X. Meng, L.L. Wu, and H.J. Zhang, *Adv. Func. Mater.Func. Mater.* 24, 4034 (2014).
12. S.-N. Zhao, G. Wang, D. Poelman, and P.V.D. Voort, *Materials* 11, 572 (2018).
13. M. Mon, A. Pascual-Álvarez, T. Grancha, J. Cano, J. Ferrando-Soria, F. Lloret, J. Gascon, J. Pasán, D. Armentano, and E. Pardo, *Chem. Eur. J.. Eur. J.* 22, 539 (2016).
14. X. Meng, H.-N. Wang, S.-Y. Song, and H.-J. Zhang, *Chem. Soc. Rev.* 46, 464 (2017).
15. W. Shang, C. Zeng, Y. Du, H. Hui, X. Liang, C. Chi, K. Wang, Z. Wang, and J. Tian, *Adv. Mater.* 29, 1604381 (2017).
16. J. Deng, K. Wang, M. Wang, P. Yu, and L. Mao, *J. Am. Chem. Soc.* 139, 5877 (2017).
17. T.N. Tu, M.V. Nguyen, H.L. Nguyen, B. Yuliarto, K.E. Cordova, and S. Demir, *Coord. Chem. Rev.. Chem. Rev.* 364, 33 (2018).
18. C. Gomes Silva, I. Luz, F.X. LlabresiXamena, A. Corma, and H. García, *Chem. A Eur. J.* 16, 11133 (2010).
19. J. He, J. Wang, Y. Chen, J. Zhang, D. Duan, Y. Wang, and Z. Yan, *Chem. Commun.Commun.* 50, 7063 (2014).
20. Y.-P. Yuan, L.-S. Yin, S.-W. Cao, G.-S. Xu, C.-H. Li, and C. Xue, *Appl. Catal. BCatal. B* 168, 572 (2015).
21. T. Musho, J. Li, and N. Wu, *Int. J. Quantum Chem.* 116, 1153 (2016).
22. J.D. Xiao, Q. Shang, Y. Xiong, Q. Zhang, Y. Luo, S.H. Yu, and H.L. Jiang, *Angew. Chem. Int. Ed.. Chem. Int. Ed.* 55, 9389 (2016).
23. A. Asyikin, M. Halimah, A. Latif, M. Faznny, and S. Nazrin, *J. Non-Cryst. SolidsCryst. Solids* 529, 119777 (2020).
24. A.S. Dezfuli, M.R. Ganjali, and H.R. Naderi, *Appl. Surf. Sci.* 402, 245 (2017).
25. P. He, X.-Y. Yu, and X.W. Lou, *Angew. Chem. Int. Ed.. Chem. Int. Ed.* 56, 3897 (2017).
26. J. Li, J. Song, B.-Y. Huang, G. Liang, W. Liang, G. Huang, Y. Qi Jin, H. Zhang, F. Xie, J. Chen, N. Wang, Y. Jin, X.-B. Li, and H. Meng, *J. Catal.Catal.* 389, 375 (2020).
27. M. Athar, M. Fiaz, M.A. Farid, M. Tahir, M.A. Asghar, S. ul Hassan, and M. Hasan, *ACS Omega* 6, 7334 (2021).
28. A. Aijaz, J. Masa, C. Rösler, W. Xia, P. Weide, A.J.R. Botz, R.A. Fischer, W. Schuhmann, and M. Muhler, *Angew. Chem. Int. Ed.. Chem. Int. Ed.* 55, 4087 (2016).
29. G.-L. Zhuang, Y.-F. Gao, X. Zhou, X.-Y. Tao, J.-M. Luo, Y.-J. Gao, Y.-L. Yan, P.-Y. Gao, X. Zhong, and J.-G. Wang, *Chem. Eng. J.* 330, 1255 (2017).
30. H. Meng, Z. Ren, S. Du, J. Wu, X. Yang, Y. Xue, and H. Fu, *Nanoscale* 10, 10971 (2018).
31. J. Lv, X. Yang, H.-Y. Zang, Y.-H. Wang, and Y.-G. Li, *Mater. Chem. Front.* 2, 2045 (2018).
32. Y.R. Zheng, M.R. Gao, Q. Gao, H.H. Li, J. Xu, Z.Y. Wu, and S.H. Yu, *Small* 11, 182 (2015).
33. X. Wang, L. Yu, B.Y. Guan, S. Song, and X.W. Lou, *Adv. Mater.* 30, 1801211 (2018).
34. M. Xie, L. Yang, Y. Ji, Z. Wang, X. Ren, Z. Liu, A.M. Asiri, X. Xiong, and X. Sun, *Nanoscale* 9, 16612 (2017).
35. J.-B. Tan and G.-R. Li, *J. Mater. Chem. A* 8, 14326 (2020).
36. K. Lankauf, K. Cysewska, J. Karczewski, A. Mielewczyk-Gryń, K. Górnicka, G. Cempura, M. Chen, P. Jasiński, and S. Molin, *Int. J. Hydrogen Energy* 45, 14867 (2020).
37. X. Huang, H. Zheng, G. Lu, P. Wang, L. Xing, J. Wang, and G. Wang, *ACS Sustain. Chem. Eng.* 7, 1169 (2019).
38. Q. Qian, Y. Li, Y. Liu, L. Yu, and G. Zhang, *Adv. Mater.* 31, 1901139 (2019).
39. Z. Tao, T. Wang, X. Wang, J. Zheng, and X. Li, *ACS Appl. Mater. Interfaces* 8, 35390 (2016).
40. X. Wang, X. Huang, W. Gao, Y. Tang, P. Jiang, K. Lan, R. Yang, B. Wang, and R. Li, *J. Mater. Chem. A* 6, 3684 (2018).
41. V. Charles, Y. Yang, M. Yuan, J. Zhang, Y. Li, J. Zhang, T. Zhao, Z. Liu, B. Li, and G. Zhang, *New J. Chem.* 45, 14822 (2021).
42. J.-G. Kang, B.-K. Min, and Y. Sohn, *J. Mater. Sci.* 50, 1958 (2015).
43. X. Zhang, Y. Zhang, T. Wang, Z. Fan, and G. Zhang, *RSC Adv.* 9, 24802 (2019).
44. M. Aghajanzadeh, M. Zamani, H. Molavi, H. KhieriManjili, H. Danafar, and A. Shojaei, *J. Inorg. Organometal. Polym. Mater.* 28, 177 (2018).
45. H.R. Abid, J. Shang, H.-M. Ang, and S. Wang, *Int. J. Smart Nano Mater.* 4, 72 (2013).
46. R.S. Das, S.K. Warkhade, A. Kumar, and A.V. Wankhade, *Res. Chem. Intermed.Intermed.* 45, 1689 (2019).
47. J. Zeng, Z. Li, H. Peng, and X. Zheng, *Colloids Surf. A* 560, 244 (2019).
48. C.C. McCrory, S. Jung, J.C. Peters, and T.F. Jaramillo, *J. Am. Chem. Soc.* 135, 16977 (2013).

49. J. Masud, S. Umapathi, N. Ashokaan, and M. Nath, *J. Mater. Chem. A* 4, 9750 (2016).
50. M. Ali and E. Pervaiz, *Mol. Catal.* 519, 112136 (2022).